Reversible densification in nano-Li 2 MnO 3 cation disordered rock-salt Li-ion battery cathodes

Maria Diaz-Lopez, Philip Chater, Yves Joly, Olivier Proux, Jean-Louis F Hazemann, Pierre Bordet, Valérie Pralong

To cite this version:

Maria Diaz-Lopez, Philip Chater, Yves Joly, Olivier Proux, Jean-Louis F Hazemann, et al.. Reversible densification in nano-Li 2 MnO 3 cation disordered rock-salt Li-ion battery cathodes. Journal of Materials Chemistry A, 2020, 8 (21), pp.10998-11010. 10.1039/d0ta03372c. hal-02906320

HAL Id: hal-02906320

https://hal.science/hal-02906320

Submitted on 21 Sep 2020

Journal of
Materials Chemistry A

ROYAL SOCIETY
OF CHEMISTRY

PAPER

View Article Online
View Journal | View Issue

Check for updates

Cite this: *J. Mater. Chem. A*, 2020, **8**, 10998

Reversible densification in nano-Li_2MnO_3 cation disordered rock-salt Li-ion battery cathodes†

Maria Diaz-Lopez, *[a,b] Philip A. Chater, [b] Yves Joly,[c] Olivier Proux, [c] Jean-Louis Hazemann, [c] Pierre Bordet[c] and Valerie Pralong [d]

Received 25th March 2020
Accepted 8th May 2020

DOI: 10.1039/d0ta03372c

rsc.li/materials-a

The full structure of nano-Li_2MnO_3 with superior reversible capacities of 290 mA h g^{-1} for over 10 cycles was investigated by neutron and X-ray total scattering, which demonstrate that contrary to previous claims, a phase transformation occurs during synthesis forming a disordered cubic MnO-type rock-salt with nanodomains of Li/Mn layering of ~1 nm. A comprehensive study of the structural and charge evolution combining *in operando* X-ray total scattering with advanced spectroscopic methods at the Mn K-edge such as High Energy Resolved Fluorescence Detected XANES, EXAFS and Emission Spectroscopies including main and valence-to-core transitions, point to a lattice densification with an effective loss of Li_2O, with the subsequent electrochemical activation of Li_2O as the main responsible mechanism for the exchanged capacity. Interestingly, and unlike previous studies, no capacity losses could be associated to the material's densification.

Introduction

The increasing demand for higher energy density batteries continues to foster research on cathode materials with superior capacities to the current state-of-the-art ranging from 140 (in $LiCoO_2$)[1] to 200 mA h g^{-1} (in $LiNi_{0.8}Mn_{0.1}Co_{0.1}O_2$).[2] Significant improvement of the cathode specific capacity has been realized in Li-rich layered oxides xLi_2MnO_3 $(1-x)LiMO_2$,[3] where M is a 3d transition metal (TM), offering extra capacities beyond the limit of conventional TM redox reactions. These composites deliver capacities as high as 250 mA h g^{-1} (ref. 4) when charged to a high potential (~4.5 V *vs.* Li/Li^+) that activates charge compensation mechanisms alternative to unfavourable TM redox reaction involving $Mn^{4+}_{oct}/Mn^{5+}_{oct}$ in the over-lithiated Li_2MnO_3 component.

Several studies have focused on the performance of Li_2MnO_3 (ref. 5) to better understand this extra capacity which has been partly attributed to H^+ for Li^+ substitution[6–8] and more notably to oxygen redox reactions.[9,10] Anionic redox reactions in Li_2MnO_3 are accompanied by the irreversible evolution of O^{2-} at the particle surface into gaseous O_2 and superoxide radicals ($O_2^{\bullet-}$). Part of the O_2 released is removed from the cell triggering structural reorganization, such as phase segregation (gradual transformation to spinel with cycling)[11,12] or particle densification with diffusion of transition metal ions from surface to bulk where they occupy vacancies created by Li removal.[13] Highly reactive $O_2^{\bullet-}$ radicals can react with the carbonate solvent to form Li_2CO_3 and Li_2O decomposition products.[14] As a result, while exhibiting excellent initial capacities, Li-rich layered cathodes suffer from voltage fade and poor rate capabilities. In spite of significant efforts directed to avoid the irreversible evolution of O^{2-} and capacity fade in Li_2MnO_3 and xLi_2MnO_3 $(1-x)LiMO_2$ composites[15] through material processing and coating,[16] this remains an issue to be resolved prior to wider application of these systems.

Interestingly, unfavourable O_2 evolution is overcome in isostructural compounds to Li_2MnO_3 with 4d (Li_2RuO_3 (ref. 17)) and 5d (Li_2IrO_3 (ref. 18)) TMs, where reversible anionic redox is hypothesized to be stabilized by the formation of 'peroxo-like' 2.5 Å O–O dimers. Reversible oxygen redox have also been proposed for $Li_{2-x}Ir_{1-y}Sn_yO_3$ based on peroxide 1.4 Å O–O dimers bridging Ir and Sn cations, which are closer to the range of bond lengths of typical peroxide species.[19]

Within the last few years, superior capacities (200–350 mA h g^{-1}) have been observed in Li-rich cubic cation disordered rock-salts owing to the low energetic percolation of lithium diffusion paths associated with a high Li : TM ratio. This emerging new family of cathode materials show no obvious structural changes involving complex phase transformations that could eventually lead to particle cracking and battery failure upon extensive cycling. These promising features have motivated extensive work on these materials and several Li-rich disordered rock-salts have been reported,[20–22] where the highest capacities have been observed in $Li_{1.3}Nb_{0.3}Mn_{0.4}O_2$ (ref. 23)

---

[a] *ISIS Facility, STFC Rutherford Appleton Laboratory, Didcot, OX11 0QX, UK. E-mail: maria.diaz-lopez@stfc.ac.uk*

[b] *Diamond Light Source Ltd, Diamond House, Harwell Science and Innovation Campus, Didcot OX11 0DE, UK*

[c] *Grenoble Alpes Univ., CNRS, Inst. Neel, 38000 Grenoble, France*

[d] *Normandie Univ., Ensicaen, Unicaen, CNRS, Crismat, 14000 Caen, France*

† Electronic supplementary information (ESI) available. See DOI: 10.1039/d0ta03372c

(250 mA h g^{-1}), $Li_{1.2}Ti_{0.4}Mn_{0.4}O_2$ (ref. 24) (300 mA h g^{-1}) and $Li_4Mn_2O_5$ (ref. 25) (350 mA h g^{-1}). The versatility of these phases provides further scope to explore multivalent TMs, anionic redox and mixed (O^{2-}/F^-) systems which may lead to improved performance.

In a previous work, we reported the reduction of the particle size in the range of 10 nm (ref. 26) in layered Li_2MnO_3 (space group *C*2/*m*) by high-energy milling with no change of the space group symmetry. Nanostructured Li_2MnO_3 (hereafter referred to as nano-Li_2MnO_3) features improved capacity (290 mA h g^{-1}) and reduced fading (200 mA h g^{-1} retained after over ten cycles)[26] over its micro-structured counterpart which displays a 50% capacity drop over the first five cycles.[27] Upon cycling, a phase transformation into a cubic disordered MnO-type rock-salt was determined by *ex situ* electron diffraction of electro-synthesized $Li_{0.5}MnO_3$ charged to 4.5 V, although no plateau characteristic of a phase transformation could be identified in the electrochemical curve.

In the present study, average and local structural studies involving combined neutron and X-ray total scattering demonstrate that, contrary to previous claims,[26] a phase transformation occurs during the nanostructuring of Li_2MnO_3, forming a disordered cubic MnO-type rock-salt structure analogous to that of $Li_4Mn_2O_5$, but with nanodomains of Li/Mn layering with a size of ~1 nm. The structure and charge evolution of nano-Li_2MnO_3 during battery cycling was characterized by a combination of techniques performed *in operando*, including X-ray total scattering and advanced X-ray spectroscopic methods performed at the Mn K-edge, such as High Energy Resolved Fluorescence Detected near-edge X-ray Absorption (HERFD-XANES), Extended X-ray Absorption Fine Structure (EXAFS) and X-ray Emission Spectroscopies (XES) including main ($k\beta_{1,3}$ and $k\beta'$) and valence-to-core or V2C ($k\beta_{2,5}$ and $k\beta''$) transitions; this is the first time these XES techniques have been reported for batteries under *in operando* conditions.

X-ray total scattering, HERFD-XANES and EXAFS reveal a solid-solution-type response, where the reversible cycling between charged and discharged states is allowed by the breathing of a cubic Mn-framework, in discordance with a phase transformation from *C*2/*m* to $Fm\bar{3}m$ from previous studies.[26] Note also that the structural evolution of nano-Li_2MnO_3 during cycling significantly differs to that of layered Li_2MnO_3 in a crystalline state, which contracts along the *c*-lattice parameter upon delithiation. The analysis of diffraction data in reciprocal space show a large structural reversibility of nano-Li_2MnO_3 with a constant structural coherence length of Li/Mn layering nanodomains. In the real space, no distribution of O–O interatomic distances was observed that could be ascribed to the recently reported peroxo-like distances proclaimed in other high capacity cathodes, such as in layered Li_2MnO_3-type structures like $(Li/Na)_2RuO_3$ (ref. 28 and 29) and Li_2IrO_3,[18] Li_3IrO_4 (ref. 30) and 3D structures like β-Li_2IrO_3.[31]

The determination of the charge compensation mechanism in nano-Li_2MnO_3 was possible by the joint analysis of HERFD-XANES and XES data. We characterized the changes of the oxidation state of Mn following the evolution of the $k\beta_{1,3}$ transition, and utilized for the first time V2C transitions to probe plausible charge compensation mechanisms involving oxygen, like bulk anionic redox or hydroxyl –OH group formation. While soft X-rays are typically used to probe the K-edges of light atoms, these are only sensitive to surface effects given their short penetration depth. Unlike soft-XAS, the V2C spectra measured with hard X-rays (~6.5 keV) are able to probe the bulk material. Moreover, this technique only detects oxygen bound to manganese, and there is no contamination to the recorded signal from oxygen present in other components of the battery, like the electrolyte. The analysis of the data was aided by *ab initio* simulations of HERFD-XANES and V2C signals using proposed structural models based on different charge compensation mechanisms, and their confrontation with the measured spectra. Our data and simulations of spectroscopy signals point to a densification mechanism with an effective loss of electrochemically active Li_2O, which produces electrons and is the main responsible for the exchanged capacity for nano-Li_2MnO_3. The oxygen evolved from the Li_2O electrochemical activation could in turn be stabilized in peroxide species at the cathode surface, or by the trapping of O_2 molecules in vacancy clusters originated during Li-extraction. Interestingly, and unlike previous studies, very small capacity losses (0–3% over the first 10 cycles)[26] could be associated with the material's densification.

Results

Structural description of pristine nano-Li_2MnO_3

The atomic structure of nano-Li_2MnO_3 was investigated by joint analysis of neutron and X-ray total scattering data to analyse both short- and long-range ordering. Rietveld refinement was used to determine how well reported crystallographic models matched to the observed average structure. The well-known Li_2MnO_3 layered model (space group *C*2/*m*) failed to produce a satisfactory fit to the observed data (R_{wp} > 10%, see Fig. S1†), which disproves previous work[26] and indicates that a structural transformation occurs during the mechanochemical synthesis of nano-Li_2MnO_3 by the ball milling of microstructured Li_2MnO_3. A model based on a rock-salt MnO-type structure (space group $Fm\bar{3}m$) with modified occupancy values to include Li on the Mn site produced a good fit to the neutron data, but several broad reflections in the X-ray diffraction pattern could not be indexed with the cubic $Fm\bar{3}m$ space group (Fig. S1†). These reflections were attributed to the formation of a short-range ordered superstructure formed from ordering alternating layers of Li and Mn cations into alternating (111) planes in the rock-salt structure, as previously reported in $Li_xNi_{2-x}O_2$.[32] The chemical ordering of Li and Mn is described by the rhombohedral space group $R\bar{3}m$, as shown in Fig. 1.

The rhombohedral model in Fig. 1 enables the simultaneous description of both cubic $Fm\bar{3}m$ reflections from the rock salt structure, and the $R\bar{3}m$ short-range ordered supercell peaks from cation ordering.[32] In the hexagonal unit cell description, reflections deriving from the cubic structure have Miller indices with even values of l (hkl_{even}), whereas hexagonal reflections that are forbidden in the cubic unit cell, but arise due to nanodomains of Li and Mn layering, exhibit odd values of l (hkl_{odd}).

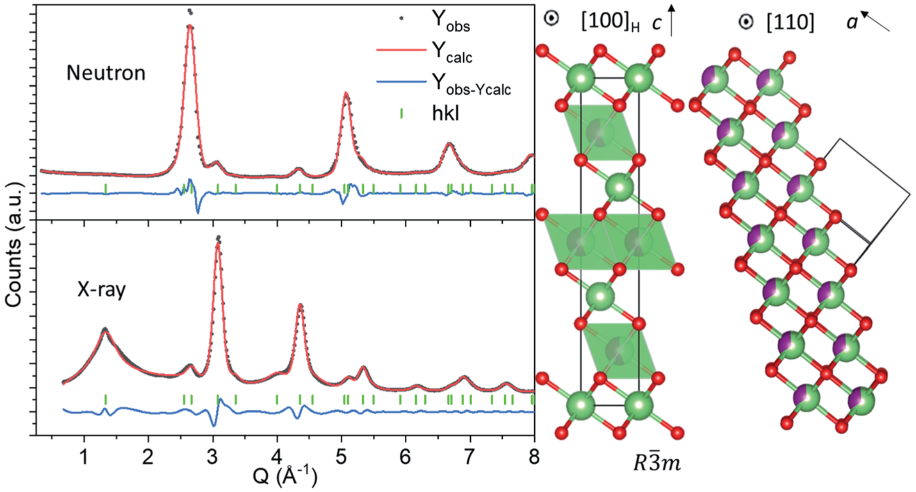

Fig. 1 (Left) Joint Pawley Fitting of neutron and X-ray data using the layered Li_2MnO_3 structure with space group $R\bar{3}m$ ($R_{wp} = 3.6\%$). (Middle) $R\bar{3}m$ model featuring chemical ordering of Li and Mn into alternating rock-salt (111) planes with space group $Fm\bar{3}m$ (Right). Green, purple and red spheres denote Li, Mn, and O atoms, respectively.

Both sets of broad and sharper reflections were fitted using a single structural model, where the *hkl*-dependent peak broadening was modelled to evaluate the crystallite size of the cubic and hexagonal sublattices. The sample size was calculated using the double-Voigt approach[33] to estimate the volume-weighted column height separated into L_{hex} and L_{cub} components for hkl_{odd} and hkl_{even} reflections, respectively. The refined value of L_{hex} of 1.2(6) nm accounts for the volume weighted length of chemical coherence of the layered hexagonal ordering, and L_{cub} = 3.8(4) nm represents the total volume weighted crystallite size of the nanostructured material, which is independent of the layered ordering. This refinement approach allowed us to quantify the extent of Li and Mn layering as approximately equal to the length of the *c* lattice parameter of the $R\bar{3}m$ model ($c_{hex} = 14.14157(6)$ Å) in Fig. 1, and is therefore a very short-range phenomena. It is important to note that the growth of this short-range layered ordering may occur along any of the [111] rock-salt directions, with coherent cubic domains between them. This structural difference between nano-Li_2MnO_3 and its microstructured counterpart may be in part responsible for the increased capacity and reversibility in this material, as opposed to nanostructuring alone.

Details of the short-range structure can be revealed by studying the pair distribution function (PDF) data. Simulation of the short *r*-range of the PDF ($r < 10$ Å) using the refined average model produced a large mismatch to the observed data in Fig. S2,† indicating a high degree of local atomic rearrangement in this material. The study of the local structure in cation disordered rock-salts is particularly challenging due to the overlap of all cation–cation, oxygen–oxygen partial PDFs and is beyond the scope of this work; a future study will focus on structural modelling *via* fitting of EXAFS, X-ray and neutron total scattering data by Reverse Monte Carlo methods using a modified version of the RMCProfile software,[34] allowing the refinement of multiple Bragg data and where the new *hkl*-dependent peak shape functions formerly introduced have been implemented. In the present study, the evolution of the local structure of nano-Li_2MnO_3 during cycling was interpreted by the curve fitting and PDF simulations using small clusters of LiO_6 and MnO_6 polyhedra and is introduced in the following section.

Bulk structural evolution during battery cycling

Rietveld refinement of total scattering data collected during cycling (Fig. 2) showed a continuous evolution of the lattice parameters that mirrors the shape of the electrochemical curve, indicative of solid solution behaviour. The cell parameter of the cubic sublattice, a_{cubic}, contracted from 4.0741(2) to 4.054(2) Å with the extraction of ~1.5 Li during the first charge to 4.5 V, and re-expanded to 4.101(2) Å during the discharge to 2 V. The solid solution response, contradicting previous claims,[26] is in congruent with the absence of characteristic plateaus in the electrochemical curve associated with phase transformations, and further supports our finding that the structure of pristine nano-Li_2MnO_3 corresponds to that of a cation disordered rock-salt structure with nanodomains of Li/Mn layering. The isotropic breathing of nano-Li_2MnO_3 is characteristic of cation disordered rock-salts, and is markedly different to the microstructured compound where the contraction of the cell occurs predominantly along the stacking direction.[35]

The evolution of all refined parameters with cycling is given in Fig. S3.† The correlation length for the cubic sublattice, L_{cub} = 3.3(2) nm, remained constant during cell charge/discharge. No significant differences in the profile of hkl_{odd} reflections were observed; however a large overlap between the most intense hkl_{odd} 003 reflection and the cell backgrounds (see diffraction data from PFA cell and carbon black additive in Fig. S3†) meant that the correlation length for the hexagonal sublattice L_{hex} could not be accurately refined and was fixed to the value obtained the joint neutron and X-ray refinement of pristine nano-Li_2MnO_3 (L_{hex} = 1.2 nm). The absence of major

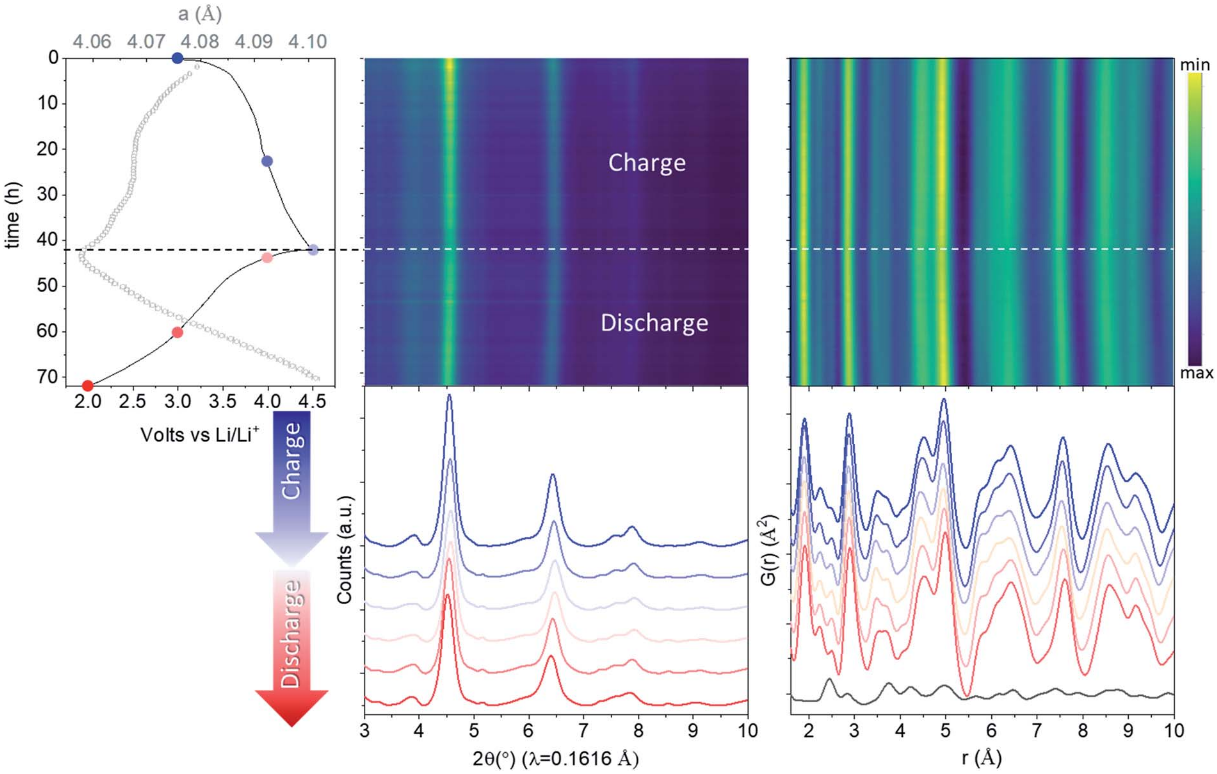

Fig. 2 *In operando* nano-Li_2MnO_3 evolution with cycling characterized by X-ray total scattering. From left to right: electrochemical performance (solid line) overlaid with lattice parameters from a sequential Rietveld refinement (grey empty circles with error bars), reciprocal and real space (PDF) total scattering data. The PDF of carbon black additive to aid electronic conductivity of the electrode is provided at the bottom of the figure. See Fig. S3† for the evolution of all refined parameters and fits. Charge data is given in blue (from dark to light) and discharge in red (from light to dark).

structural- or microstructural-rearrangements combined with good structural reversibility are both highly desirable features for cycling reversibility and capacity retention of cathode materials.

The evolution of the average structure in nano-Li_2MnO_3 resembles that of the non-stoichiometric cation disordered rock-salt of composition $Li_4Mn_2O_5$,[25] in that in both compounds the extraction and insertion of lithium is accompanied by the breathing of the Mn cubic framework. The similarities between the evolution of the local and average structures in $Li_4Mn_2{}^{3+}O_5$ and $Li_2Mn^{4+}O_3$ are remarkable, given that different charge compensation mechanisms are expected in these cathode materials.

X-ray PDF data was used to extract the Mn–O distance during cycling (Fig. 2). Only very minor changes in the Mn–O distance were observed, evolving from 1.907(2) Å for pristine, 1.894(2) Å for charged and 1.908(2) Å for discharged phases, all of which are consistent with the expected $r(\mathrm{Mn}_{\mathrm{VI}}^{4+}-\mathrm{O}_{\mathrm{VI}}^{2-})$ of 1.93 Å.[36] This constant Mn^{4+} oxidation state may be expected from ligand field theory considerations, where the splitting in energy of Mn^{5+} d-orbitals in an octahedral configuration is substantially larger than for tetrahedral. In absence of Mn redox, and alternative charge compensation mechanism must be found.

PDF data can also provide information on the local oxygen environment and so potential for anionic redox mechanisms involving oxygen were investigated. Reversible anionic redox have been attributed to the sharing of one electron hole between two oxygen atoms *via* formation of peroxo-like $(O_2)^{3-}$ species in Li_2RuO_3 and Li_2IrO_3, which are isostructural with the crystalline phase of Li_2MnO_3 (space group *C*2/*m*). O–O dimers approximately 2.3–2.5 Å apart have been proposed based on Ru K-edge EXAFS,[28] Bragg diffraction,[31] and transmission electron microscopy (TEM). Unlike PDF analysis, these techniques are not direct probes of O–O distances. (i) EXAFS is a model dependent technique where interatomic distances appear shifted due to the scattering phase-shift, (ii) Bragg diffraction quantifies the distance between mean atomic positions $d_{\langle O\rangle-\langle O\rangle}$ different to the actual distribution of interatomic distances $d_{\langle O-O\rangle}$, and (iii) projection limitations exist by TEM. Therefore, large uncertainties surround the estimated O–O distances in peroxo-like dimers. In the absence of Mn redox, we consider whether a charge compensation mechanism accounting for ∼1.5Li during charge may be solely attributed to anionic redox. Such a compensation mechanism would change the oxidation state of all oxygen anions from 2^- to 1.5^- to give $Li_{0.5}Mn^{4+}O_3{}^{1.5-}$, where all the oxygen atoms could become dimerized following the charge compensation mechanisms hypothesized for Li_2RuO_3 and Li_2IrO_3. At such a high concentration of O–O dimers, their contribution to the total XPDF signal is not negligible. To demonstrate the impact of dimer formation, XPDF data was simulated for MnO_6 containing three dimerized O–O pairs at 2.3 Å and 1.4 Å for peroxo-like and peroxo bridges[19] respectively (Fig. S4†). The formation of 'peroxo-like' dimers significantly changes the O–O partials within MnO_6 which in turn gives rise to the formation of new peaks with detectable/measurable intensities at the new O–O distances (at 2.3 and 1.4 Å in Fig. S4†), and also affects the width and intensity of the peak at ∼2.9 Å comprising overlapped cation–cation and O–O distances.

The 1.4–2.5 Å range in the observed *in operando* PDF data were carefully examined (Fig. 3) and the evolution of peak width and intensity were characterized by the fitting of five Gaussian functions (Fig. S5†). The superposition of PDFs for the peaks at ∼1.4 and 2.5 Å attributed to C–C distances from the carbon black additive, rules out the O–O evolution at these distances. The intensity of the Li–O peak at ∼2.3 Å decreases during charge and increases during discharge, as expected for the reversible extraction–reincorporation of lithium. No increase in the intensity of this peak at the 4–4.5 V range characteristic of anionic redox activity was observed that could be attributed to the formation of O–O dimers in significant concentrations. For the Mn–O peak at ∼1.9 Å, a decrease in width was observed upon charging, corresponding to a more ordered local structure, but the integrated intensity remained constant. The absence of peroxo-like or peroxo bridge distances is further supported by the constant refined width of the peak at ∼2.9 Å attributed to cation–cation and O–O distances overlapped in the rock-salt structure. As previously shown by our simulations, the O–O pairs contribute to 20% of the intensity of this peak, and dimer formation would entail a significant change of its width and intensity, which was not observed experimentally. It can be concluded that PDF data does not support anionic redox process stabilized by the formation of peroxo-like or peroxo bridges in nano-Li_2MnO_3.

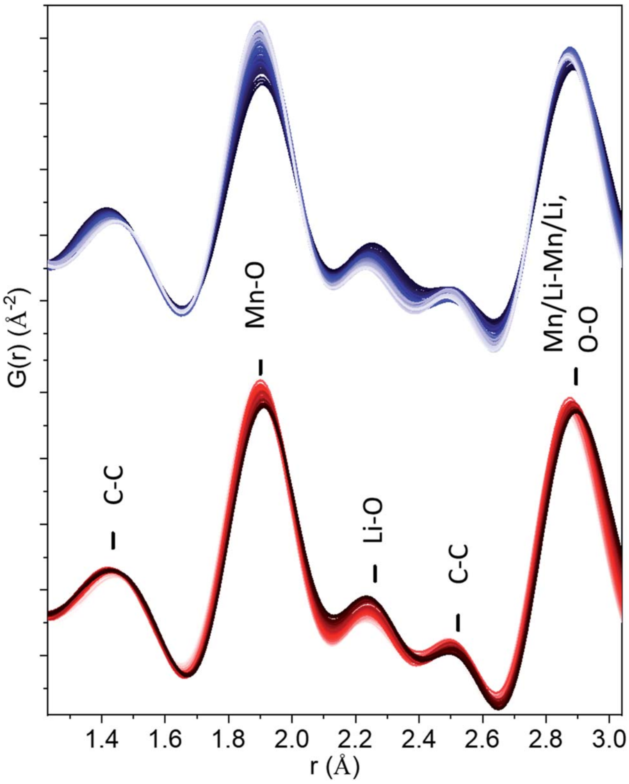

Fig. 3 Short *r*-range of PDFs in the figure demonstrating the absence of peroxide $(O_2)^{2-}$ or peroxo-like $(O_2)^{3-}$ distances. Charge data is given in blue (from dark to light) and discharge in red (from light to dark).

Local structure around Mn during cycling

The evolution of the coordination environment around MnO_6 in nano-Li_2MnO_3 was further characterized by *in operando* Mn K-edge HERFD-XANES, which is highly sensitive to structural changes around Mn cations. As established for known Mn standards,[37] different coordination environments of 3d transition metals show very different pre-edges, and these features were used to characterize changes in the coordination number and centrosymmetricity of Mn in nano-Li_2MnO_3.

The evolution of the HERFD-XANES data measured *in operando* during the first charge to 4.5 V and discharge to 1.2 V are shown in Fig. 4. The most significant change in the spectra correspond to the progressive fading of the shoulder at ∼6550 eV. First principle calculations were performed using the proposed $R\bar{3}m$ structural model and an $Fm\bar{3}m$ models where suitable Li and Mn compositions were randomly distributed on the same site (Fig. 5); these calculations demonstrated that the intensity of the shoulder feature correlates with the amount of Li on the Mn lattice, as determined previously by first principle calculations on $Li_4Mn_2O_5$.[37] The absence of this shoulder simulated at a charged composition of $Li_{0.5}MnO_3$ is reflected in the observed data at 4.5 V and the reappearance of this feature at the same energy during discharge indicates a high reversibility, in agreement with *in operando* total scattering data. Note that the apparent shift of the edge to higher energy values during charge is not caused by an increased Mn oxidation state, but instead by the expansion of the spectra on the energy scale due to the contraction of the lattice in accordance with Natoli's rule, and in agreement with the smaller lattice parameter observed from Rietveld refinement.

Significant changes of the pre-edge region of the XANES spectra are shown in Fig. 5. In the pristine material, two peaks can be distinguished at 6541 and 6543 eV, which are ∼2 eV apart as expected for the energy gap between the t_{2g} and e_g states of a regular octahedral environment. Upon charging, the overall intensity of the pre-edge increases, and the relative intensity between the two peaks gradually changes until they become approximately equal intensity in the charged state. Such an observation points to a reduction in centrosymmetricity of the Mn centres, which become more distorted/irregular during charge. This reduction is centrosymmetricity is completely reversible upon discharge. Since no meaningful differences were apparent between the calculated spectra using $R\bar{3}m$ and $Fm\bar{3}m$ models from XANES simulations, only the $Fm\bar{3}m$ model, which allowed more facile composition changes to be investigated, was retained for further spectroscopic analyses in the following sections.

The evolution of the environment around manganese that could be responsible for the changes in the shape and intensity

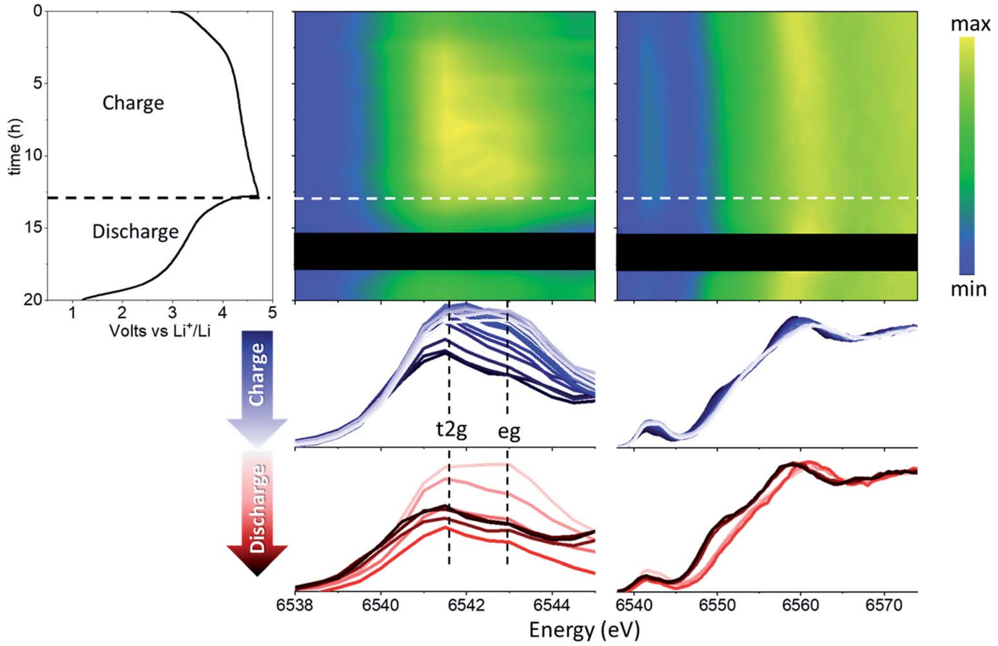

Fig. 4 Nano-Li_2MnO_3 evolution with cycling characterized by advanced XAS methods. From left to right: electrochemical performance and contour plots of the magnified pre-edge region and HERFD-XANES. The black square corresponds to missing data due to beam loss. The bottom figures show superimposed spectra for charging (blue) and discharging (red).

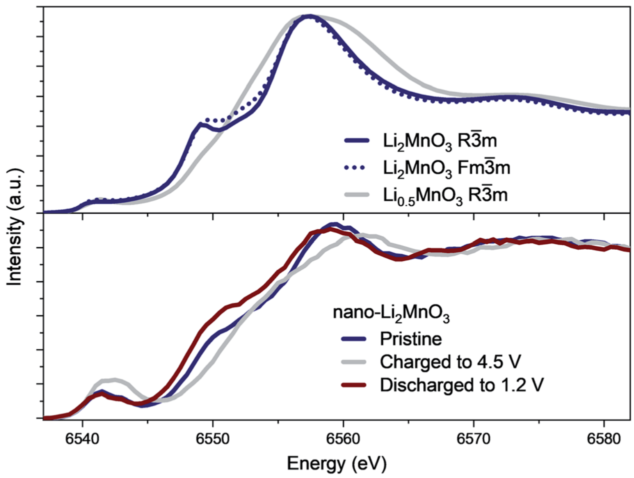

Fig. 5 XANES simulations using $R\bar{3}m$ and $Fm\bar{3}m$ models proposed from Rietveld refinement for pristine nano-Li_2MnO_3 and charged to 4.5 V, showing both structural models are in agreement with XANES spectra and the shoulder at ~6550 eV originates from the presence of Li on the Mn lattice in Li-rich compositions. The experimental data for the same energy range is given below for comparison.

of the HERFD-XANES pre-edge were investigated *ex situ* using EXAFS collected at the start (pristine) and end of the first charge cycle (charged to 4.5 V). A comparison with *in operando* data collections is provided in Fig. S6,† showing an excellent agreement. Fig. S7† compares the $\chi(k)$ and Fourier transform (FT) $\chi(r)$ signals for the pristine and charged to 4.5 V compositions with a significant damping of the higher order shells (>3 Å) in $\chi(r)$, a common feature in nanostructured materials (*e.g.*, $Li_4Mn_2O_5$,[37] α-MnO_2 (ref. 38)) and attributed to a high degree of structural disorder.

The average structures from Rietveld refinements were used as starting configurations for the least-square fitting of EXAFS data, to quantitatively evaluate short-range order structural parameters. Three single scattering paths including O and Mn shells were refined, while Li shells were not included in the refinement due to the small scattering power of this atom. Interatomic distances (R) and mean square displacements (σ^2) were refined for all paths. However, due to the high degree of correlation amongst path degeneracies (N_{degen}) and σ^2, N_{degen} were fixed to known values, which produced a good fit to the data for pristine nano-Li_2MnO_3 ($R_{\mathrm{wp}} = 2.8\%$, Fig. 6). However, for charged nano-Li_2MnO_3, N_{degen} were fixed to known values for Mn–O and Mn–O2 shells (see Table S1†), while those of Mn–Mn were allowed to vary. The interested reader is referred to Page S14† for a full discussion of the fitting parameters. The refinement of Mn–Mn path degeneracy was key for the obtainment of a good fit for the charged sample. The fit improved from $R_{\mathrm{wp}} = 4.6$ to 2.9%, when the refined mean path degeneracy varied from 2 in the Rietveld model to 5 ± 2. This result could be correlated to the migration of Mn cations to the vacancies generated by the extraction of ~1.5 Li per formula unit amounting to 50% of the cations in nano-Li_2MnO_3. Such an increase in the Mn–Mn path degeneracy will imply the occupation of 25% of the generated cation vacancies by Mn. Cation rearrangement and densification processes are not uncommon amongst positive electrode materials,[39] and have been previously reported in other Li–Mn–O systems including crystalline Li_2MnO_3 (ref. 11) and $Li_4Mn_2O_5$.[37] However, unlike for the non-stoichiometric $Li_4Mn_2O_5$ rock-salt, no oxygen vacancies are

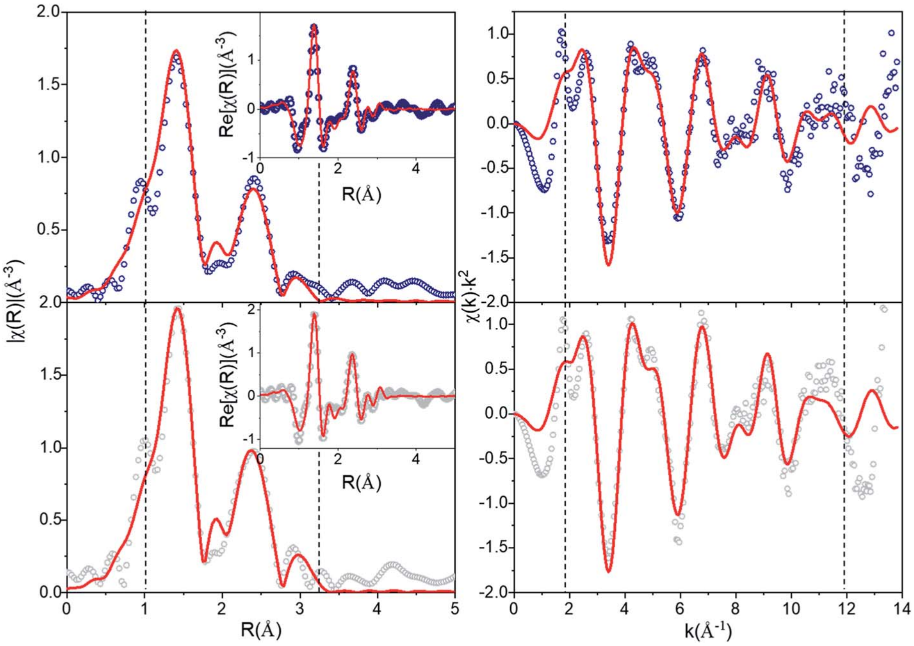

Fig. 6 EXAFS fitting of nano-Li_2MnO_3 ($R_{wp} = 2.8\%$) and charged nano-$Li_{0.5}MnO_3$ to 4.5 V (2.9%). EXAFS data (circles) and best fits (red line). Left: magnitude of FT $\chi(r)k^2$ with the inset showing the real part; right: $\chi(k)k^2$. Dashed vertical lines indicate the fit range ΔR and data range Δk of [1–3.125] Å and [1.9–12] $Å^{-1}$, respectively.

present in stoichiometric nano-Li_2MnO_3 with a fully occupied cation and oxygen sublattices, where cation densification would imply an effective extraction of Li_2O from the material.

A comparison of the refined distances with those from the average model is given in Table S1.† For both samples, refined Mn–Mn and Mn–O distances match those of the average structure within errors, while there is a shortening of the average of Mn–O bond length that amounts to 92% of the expected value, and are in good agreement with Mn–O distances observed in the PDF and expected for these atoms in oxidation states Mn^{4+} and O^{2-}. A shortening of the Mn–O bonds that could result from the change in the oxidation state of Mn and/or O was detected neither by XPDF nor by EXAFS.

In summary, the evolution of HERDF-XANES and total scattering data measured *in operando* demonstrated an excellent structural reversibility of the nano-Li_2MnO_3 cathode during the first (dis)charge cycle with a solid-solution type response allowed by the breathing of a cubic Mn-framework, in agreement with *in operando* total scattering data evolution. The evolution of the short *r*-range structure studied by EXAFS, and previously by XPDF, did not show a shortening of Mn–O bonds characteristic of peroxide species with smaller radii, or significant changes in the local structure associated to the formation of 'peroxo-like', or peroxo-bridge species during the stabilization of anionic redox processes, but pointed instead to the densification of the cation sublattice. During densification, the migration of Mn cations between two octahedral sites will involve the formation of intermediate stages with Mn in different coordination environments, which will in turn explain the increased pre-edge intensity in Fig. 5. The participating charge compensation mechanisms were studied in depth by X-ray emission spectroscopies, and are discussed in the following section.

Electronic structure evolution during cycling

Note that while the position of the absorption edge or "white line" is commonly used as an indication of the oxidation state, its shape is strongly influenced by structural effects leading to large inaccuracies. We have instead determine the oxidation state of Mn with greater precision from the position of the $k\beta_{1,3}$ transition, as explained in the following section.

Redox processes were investigated through *in operando* XES by the combined interpretation of main ($k\beta'$ and $k\beta_{1,3}$) and V2C ($k\beta''$ and $k\beta_{2,3}$) transitions (Fig. 7). The kβ emission of first row TMs can be explained as a two-step process represented by the schematic diagram in Fig. 7a. The different chemical selectivity of main kβ and V2C to manganese and oxygen respectively, makes XES a powerful tool to investigate the electrochemical activity of Li-rich cathode materials with capacities beyond those expected from TM redox. The use of hard X-rays in XES or Resonant Inelastic X-ray Scattering (RIXS) provides bulk structural information, unlike techniques employing soft X-rays (*e.g.*, XPS, or light elements K-absorption edges) which are only sensitive to surface atoms and require high vacuum compatible sample environments. In addition, V2C combines both bulk sensitivity and selectivity to the detect exclusively the O bound to Mn in the active material; unlike RIXS, V2C measurements eliminate possible contamination of the spectroscopy signal with oxygen in other components of the battery, like the cell case or electrolyte. *In operando* XES data was collected using a conventional cell for XAS experiments equipped with a beryllium window.[37] While advanced spectroscopic measurements

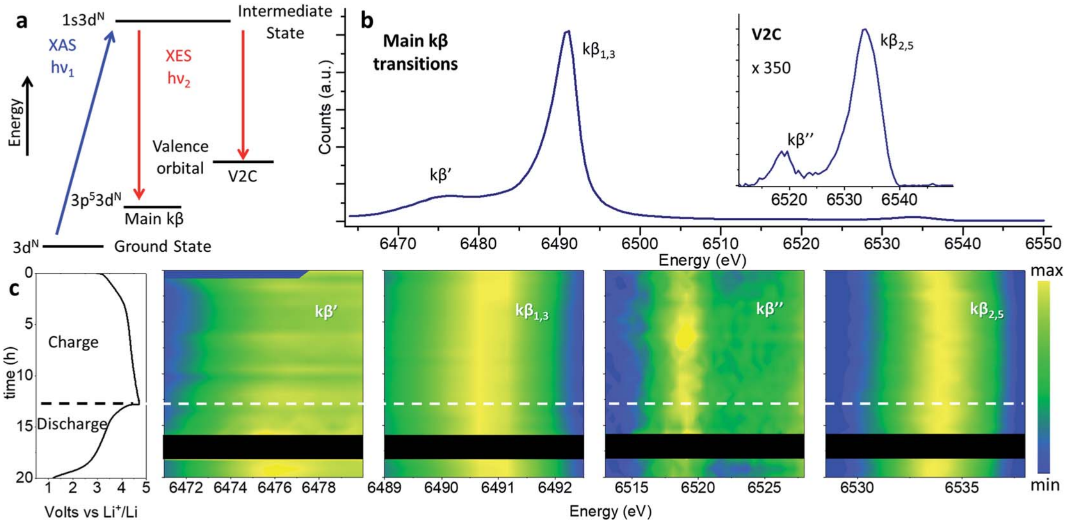

Fig. 7 Nano-Li_2MnO_3 charge evolution with cycling characterized by *in operando* XES. (a) Two-step energy schematic of main kβ and V2C transitions. (b) Whole energy range spectra for pristine nano-Li_2MnO_3. (c) From left to right: electrochemical performance and contour plots of the magnified energy regions for kβ′, $k\beta_{1,3}$, kβ″ and $k\beta_{2,5}$ transitions. Curve-fitted kβ′, $k\beta_{1,3}$, kβ″ and $k\beta_{2,5}$ energies and integrated intensities are introduced in Fig. S10.†

including HERFD-XANES and XES have been previously applied to the *in operando* characterizations of catalysts,[40] the present work constitutes the first *in operando* XES (main kβ and V2C transitions) study of Li-ion batteries.

Previously we demonstrated the use of main kβ transitions are a more accurate indication of the Mn oxidation state than XANES 1s–4p energy transitions.[37] The 3p orbitals lay deeper within the electronic shells, and as such are less dependent on structural effects than the 1s–4p transition probed at the Mn absorption K-edge. In main kβ XES, the number of unpaired 3d electrons can be indirectly inferred from magnitude of 3p–3d exchange interactions (proportional to the number of unpaired 3d electrons), given by the difference between kβ′ and $k\beta_{1,3}$ transitions. We use the comparison of the most intense $k\beta_{1,3}$ transition with those of Mn oxides with well-known oxidation states in Fig. S8 and S9† as a gauge of Mn oxidation state at different states of charge.

The main kβ spectra of pristine nano-Li_2MnO_3, as the HERFD-XANES discussed above and the V2C spectra below, are in good agreement with the MnO_2 data with the same oxidation state of manganese. During charge, a shift of $k\beta_{1,3}$ transition towards lower energy values is observed that is fully reversed during discharge, in agreement with the good structural reversibility observed for the *in operando* total scattering and HERFD-XANES data. Note the subtle variation of $k\beta_{1,3}$ energy is the only difference between the spectra, and the integrated intensities for kβ′ and $k\beta_{1,3}$, and the kβ′ energy transition remain constant during battery cycling (see Fig. S10†). As well as the number of unpaired 3d electrons, the magnitude of the 3p–3d exchange interaction depends also on the spin state and the covalency/charge-transfer contribution effects which are expected to change when chemical environment around MnO_6 centres is modified during cell (dis)charge. Due to the lower magnitude of the $k\beta_{1,3}$ shift, in comparison to the more significant differences observed when the oxidation state of Mn is varied across the different standards, this subtle energy variation was attributed to changes in the Mn–O covalency that accompany the slight shortening of Mn–O bonds during charge by $\sim$0.02 Å observed by PDF. Therefore, this analysis indicates manganese remains at a constant state of Mn^{4+}, but changes of the Mn–O covalency occur during charge and discharge processes.

Mn–O interactions were further investigated by V2C spectroscopy (including lower kβ″ and higher $k\beta_{2,5}$ energy transitions) which has a high sensitivity to the chemical environment around Mn centres. The energy separation between kβ″ and $k\beta_{2,5}$ transitions is determined by the binding energy difference between ligand-s and -p orbitals, and their intensities reflect the degree of hybridization between ligand and TM p states.[41] The lower energy kβ″ transition, which originates from ligand s molecular orbitals to TM p states, is a valuable tool for ligand identification. The energy of this kβ″ transition depends on the difference between the ligand-2s and TM-1s binding energies, and reflects the spatial overlap between ligand 2s and TM 4p/3d molecular orbitals. The kβ″ intensity is affected by the TM-ligand distance and by the coordination number of the TM. Shorter distances (*e.g.* from higher bond order or deprotonation) result in increased kβ″ intensity, with an approximate exponential dependence on distance.[42] Thus, the evolution of the kβ″ transition during cycling is able to detect changes in the charge density on the metal (Mn), ligand (O) protonation, and changes in the coordination environment of the ligand. The higher energy and more intense $k\beta_{2,5}$ originates from the transition of electrons in an occupied valence molecular orbital with mainly ligand-p and metal-p contributions (see Fig. S11†). The evolution of this signal during cycling signifies changes in the valence orbitals and TM-ligand chemical bond nature.

The evolution of k$\beta_{2,5}$ and kβ'' transitions with electrochemical cycling of nano-$LiMn_2O_3$ are given in Fig. 7. Very small changes of the peak position and intensities were observed upon cycling, which were particularly small in comparison with the much larger changes between the spectra of standard compounds of Mn in different oxidation states. During charge, the k$\beta_{2,5}$ transition increased in energy by $\sim$0.5 eV with a concurrent increase of 5% in the integrated intensity; these changes was fully reversed during discharge. No significant change in the kβ'' transition was identified by curve-fitting (Fig. S10†).

The V2C spectra were simulated using a 2 × 2 × 2 supercell of composition $Li_{21}Mn_{11}O_{32}$ built from the expansion of the proposed average model from Rietveld where the lattice parameters have been refined with a high accuracy ($a_{\text{cubic}} = 4.0741(2)$ Å), and Mn–O distances were relaxed to $\sim$1.9 Å to match the values proposed from XPDF and EXAFS analyses (Fig. S12†). These simulations reproduced the main V2C spectral features for pristine nano-Li_2MnO_3. Minor changes were observed in the V2C spectra during cycling, which we evaluate along with input from other observations in the following section.

Evaluating possible charge compensation mechanisms

The combination of observations from the above techniques allows for possible charge compensation mechanisms to be compared and appraised as an alternative to the unfavourable evolution of octahedrally coordinated manganese from Mn^{4+} to $Mn^{5+/7+}$.[43] Here we evaluate four proposed hypotheses of plausible charge compensation mechanisms in nano-Li_2MnO_3: (i) lattice densification, (ii) formation of hydroxyl groups (–OH), (iii) trapping of positively charged hydronium molecules (H_3O^+), and (iv) anionic redox.

(i) Densification. A densification mechanism was suggested by EXAFS observations. Two models have been proposed for charged compositions that have been originated from the nano-Li_2MnO_3 supercell with updated lattice parameters from Rietveld refinement ($a_{\text{cubic}} = 4.054(2)$ Å), where lithium atoms have been replaced by cation vacancies to obtain a Li : Mn ratio of 1 : 2 based on the ratio proposed by electrochemistry and ICP analyses. The V2C simulation of such model ($Li_5Mn_{10}O_{32}$), with $\sim$50% cation vacancies is given in Fig. S12.† Additionally, 23% of the cation vacancies were removed from $Li_5Mn_{10}O_{32}$ in a second 'densified' model ($Li_6Mn_{13}O_{32}$) matching the Mn–Mn path degeneracies suggested by EXAFS. Such a structural modification will imply the effective loss of 25% of oxygen in nano-Li_2MnO_3 with the effective extraction of Li_2O following the reaction:

$$Li_2MnO_3 \rightarrow 0.75Li_{2/3}\square Mn_{4/3}O_3 + 0.75Li_2O \tag{1}$$

where '□' represents a cation vacancy.

The comparison between V2C simulations of 'undensified' $Li_5Mn_{10}O_{32}$ and densified $Li_6Mn_{13}O_{32}$ in Fig. S12† shows a shift of the kβ'' and k$\beta_{2,5}$ transitions to higher energies for the 'undensified' composition by approximately 0.5 and 1 eV. This trend is also observed for Mn standards, where kβ'' and k$\beta_{2,5}$ transitions shift also by 0.5–1 eV to higher energies with the increased oxidation state of manganese, and is consistent with the higher oxidation state of Mn expected for the undensified model *vs.* the densified one. The different energy transitions between pristine and the undensified models are not experimentally observed and a much better agreement is obtained with the densified model based on EXAFS refined path degeneracies. Additionally, the lower intensity of the kβ'' transition in the undensified model correlated to the lower number of Mn neighbours around oxygen in this model, is opposite to the experimental observation with a small 5% increase of the kβ'' intensity.

(ii) Mn–OH formation. Protonation during cycling and formation of a –OH hydroxyl group has previously reported for spinel electrodes[44] and Li_2MnO_3. Charge compensation *via* the formation of hydroxyl groups would lead to the formation of $H_{1.5}Li_{0.5}MnO_3$ after the first charge to 4.5 V, giving rise to equal numbers of Mn–O and Mn–OH bonds. Upon protonation, oxygen atoms in the Mn–O network are typically relaxed 0.1 Å away from manganese in Mn–OH.[45,46] However, a different evolution of Mn–O distances have been observed by XPDF, showing a small contraction of Mn–O distances by $\sim$0.02 Å upon charging. Moreover, as previously reported in the literature,[47,48] protonated Mn–OH states give a very distinct intensity and position of the kβ'' emission signal to Mn–O. In fact, the kβ'' region of the V2C spectra has been used as a probe to distinguish the protonation state of TM bound ligands in a previous study.[47] The V2C spectra were simulated for two models with a cubic disorder rock-salt structure with compositions $\sim H_{1.5}Li_{0.5}MnO_3$ ($H_{15}Li_5Mn_{11}O_{32}$) and $Li_{0.5}MnO_3$ ($Li_5Mn_{11}O_{32}$), where Mn–OH and Mn–O distances were fixed at a constant value, as previously determined by XPDF and EXAFS refinements (see Fig. S13†). Even in these unphysical models with identical Mn–OH and Mn–O distances, our simulations show a shift of 2 eV towards lower energies occurs for both kβ'' and k$\beta_{2,5}$ transitions upon protonation of 50% of the oxygen ligands, as well as significant changes in the shape and width of the kβ'' transition. Hence, the protonation of oxygen involving the formation of hydroxyl groups is contradicted by both total scattering and spectroscopy data.

(iii) Trapped H_3O^+. Protonation and trapping of H_3O^+ molecules has previously been reported for α-MnO_2 (or Mn_8O_{16}) type materials.[49,50] α-MnO_2 has a hollandite-type structure with space group *I*4/*m*, which consists of corner and edge sharing MnO_6 octahedra with mixed oxidation states of Mn^{3+} and Mn^{4+} cations. The structure is composed of open tunnels that can accommodate the presence of cations and small molecules including K^+, Ag^+, Na^+, Mg^{2+}, $NH_4{}^+$ and H_3O^+.[49–51] This has led to tunnel structured manganese oxides being investigated in the fields of catalysis, adsorption-separation, and ion exchange.

The V2C spectral signature of trapped H_3O^+ molecule was evaluated by the simulation of V2C spectra from structural models for α-MnO_2 reported in the literature with/without H_3O^+ in Fig. S14.† These simulations show a small increase in of the kβ'' intensity, compatible with the 5% increase of the integrated intensity observed for this transition during cycling of nano-Li_2MnO_3. Similarly-sized one-dimensional tunnels to those present for α-MnO_2 2 × 2 (0.46 × 0.46 nm^2), with only a slightly smaller surface of 0.44 × 0.44 nm^2, are formed as a result of the extraction of lithium in nano-Li_2MnO_3; the surface of these voids could be further enlarged by the displacement of Mn cations away from their average positions. The large concentration of voids in charged nano-Li_2MnO_3 generated from the extraction of lithium could potentially host H_3O^+ molecules originated from electrolyte decomposition, where trapped H_3O^+ molecules compensate part of the charge exchanged upon charging following the reaction in eqn (2).

$$Li_2MnO_3 + xH_3O^+ \rightarrow (H_3O)_xLi_{2-x}MnO_3 + xLi^+ \qquad (2)$$

The participation of eqn (2) in the charge compensation of nano-Li_2MnO_3 (if any) is expected to be small, based on the reported concentration of these molecules previously reached in α-MnO_2 with a H_3O^+ to Mn ratio of 0.15 : 1. This amounts to only 10% of the 1.5 electrons per formula unit extracted over the course of the first charge. The corroboration and quantification of this charge compensation mechanism to the overall capacity could not be accurately determined by the techniques used in this work, and requires follow-up H-NMR studies.

(iv) Anionic redox. V2C spectroscopy has been a powerful tool to detect the presence of O–O bonds,[41] oxo bridges[52] and Mn-peroxo units[53] of Mn oxygen-evolving complex that revealed different spectroscopic signatures of kβ″ transitions. While significant changes between V2C transitions of Mn–O^{2-} and Mn–$(O_2)^{2-}$ bonds have been reported which showed that the kβ″ transition is split into two peaks when Mn (or other TMs) is bound to peroxo species,[41,52] the V2C spectral signature of peroxo-like species is currently unknown. Having previously ruled out the sole participation of peroxo-like dimers as a charge compensation route in nano-Li_2MnO_3 by XPDF and EXAFS, we simulated the V2C spectra for charged nano-Li_2MnO_3 structural models ($Li_6Mn_{13}O_{32}$) with O–O dimers at 2.3 Å, formerly introduced in Fig. S4b,† to (i) identify the V2C spectral signature of such defects and (ii) determine the extent to which V2C can be sensitive to a small concentration of such defects. The comparison of $Li_6Mn_{13}O_{32}$ structural models with dimerized and regular MnO_6 shows large similarities between the two practically superimposable V2C spectra (Fig. S15†). Moreover, the integrated charge for oxygen atoms in regular and dimerized MnO_6 models is also comparable, with the charge of oxygen atoms in dimerized MnO_6 models actually 8% smaller (more reduced) than for oxygen in the regular octahedral environment, or in other words, a charge variation 'Δq' in oxygen of 0.16. Thus, our calculations indicate not only that the longer O–O peroxo-like dimers at 2.3 Å could not be detected by V2C even at the largest concentrations, but also that the presence of such defects does not significantly change the integrated charge for oxygen.

From the results above, the best agreement between proposed charge compensation mechanism and observed experimental data (XPDF, EXAFS and V2C) is given by the densified model, as shown in Fig. 8 (and Table S2†). The proposed densification of the Mn sublattice implies the loss of Li_2O during the cathode charge, and has been previously reported in other cathode materials within the LiMnO system.[54,55] However, unlike previous studies, the cation densification could not be linked to unfavourable anionic redox that result in the formation of evolving $O_{2(g)}$ or $O^{\bullet-}$ radicals that in turn react with the electrolyte to produce LiOH, Li_2O_2 or Li_2CO_3 secondary phases associated with capacity drop and structural instability. The absence of undesirable secondary phases in nano-Li_2MnO_3 could be the origin of the large structural reversibility and reversible charge capacity of over 290 mA h g^{-1}.

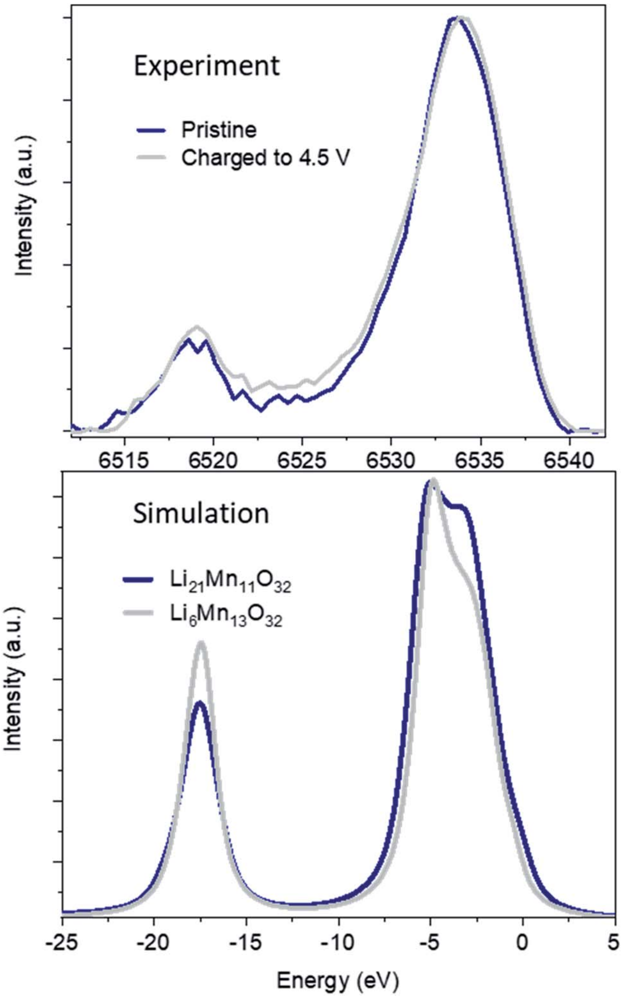

Fig. 8 Experimental (Top) and best calculated (Bottom) V2C spectra for pristine and charged nano-Li_2MnO_3.

Discussion

This comprehensive study utilising multiple techniques with different chemical and lenghtscale sensitivities have provided an unequivocal answer: no oxygen or manganese redox reactions in the bulk material or structural transitions are responsible for the charge compensation in nano-Li_2MnO_3. Instead, the observation of lattice densification points to the reversible extraction and reinsertion of Li_2O in nano-Li_2MnO_3. The absence of a Li_2O secondary phase in our data is indicative of the electrochemical activation of this compound as the main charge compensation mechanism responsible for the reversible capacity in nano-Li_2MnO_3 (see Fig. 9). This observation is in agreement with the recently reported ability of nanostructured Li–Mn–O disordered rock-salts to catalyse the electrochemical activation of Li_2O in Li_2O:Li–Mn–O nanocomposites[56] with superior first charge capacities (>1100 mA h g^{-1}) following the reactions:

$$LiO_2 \rightarrow 2Li^+ + \frac{1}{2}O_2^{\cdot-} + e^- \tag{3}$$

$$LiO_2 \rightarrow 2Li^+ + \frac{1}{2}O_2(g) + 2e^- \tag{4}$$

The reaction of highly reactive oxygen radicals formed in eqn (3) with the electrolyte at the electrode surface is known to generate $C_2O_6{}^{2-}$ ions, and finally form[57] Li_2CO_3 at the cathode surface, which causes serious problems in the cycling reversibility and repeatability as often reported for Li–O_2 batteries.[14,58] Here, the absence of Li_2CO_3 or other electrolyte decompositions products during cycling could be linked to the higher cycling reversibility of nano-Li_2MnO_3, where $C_2O_6{}^{2-}$ ions could be stabilized at the surface of nano-Li_2MnO_3, acting as an oxygen reservoir during discharge.

The formation of molecular O_2 in eqn (4) has been frequently associated with capacity losses and compositional changes on Li-rich cathode materials. Recently, House *et al.*[59] have identified reversible bulk O-redox reactions forming molecular O_2 inside $Na_{0.75}[Li_{0.25}Mn_{0.75}]O_2$ cathodes with a ribbon superstructure. During charge, the O_2 molecules are trapped in the vacancy clusters formed as a results of the Li-extraction and have no mechanism of diffusing to the surface; and during discharge, the trapped O_2 molecules may be cleaved, enabling reversible capacities.

Therefore, both (i) the stabilization of $C_2O_6{}^{2-}$ ions at the surface of the nano-Li_2MnO_3 cathode; or (ii) the trapping of O_2 molecules in vacancy clusters could be plausible charge compensation mechanisms responsible for the absence of significant formation of secondary phases at the cathode interface or electrolyte degradation during the first cycle. Further studies are needed to clarify the contribution of eqn (3) or (4), and charge compensations (i) or (ii) to the reversible electrochemical activation of Li_2O.

Note the ability to reverse the Li_2O formation reaction in nano-Li_2MnO_3 with such a large efficacy (~97% of coulombic efficiency during the first cycle) is an unprecedented observation for Li_2MnO_3 or other Li-rich cathodes. Since Li_2O is the ultimate discharged product of a Li–O cell or a hybrid Li-ion/Li–O_2 cell,[60] the possibility to reverse the formation of Li_2O by the reversible oxidative decomposition of the electrolyte is a desirable feature previously explored in other lithium metal oxides. This is the case of Li_5FeO_4 ($5Li_2O\cdot Fe_2O_3$)[60] and Li_6MO_4 ($3Li_2O\cdot MO$, M = Mn, Co)[61] compounds with an antifluorite-type structure, $CaFeO_3$,[62] $Ca_{1-x}La_xFeO_{3-\delta}$,[63] $Li_{(4-x)/3}Ti_{(2-2x)/3}Fe_xO_2$, $SrMO_{3-\delta}$ (M = Co, Fe),[64] and $Bi_2Fe_4O_9$ (ref. 65) electrodes when used in aprotic lithium or sodium cells.

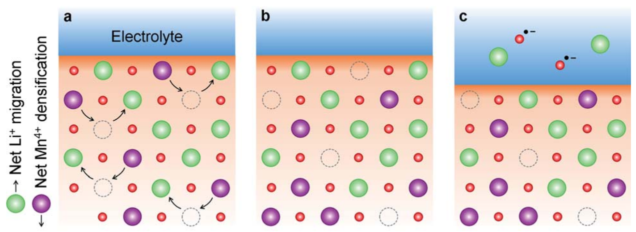

Fig. 9 Nano-Li_2MnO_3 densification followed by electrochemical activation of Li_2O. (a) Densification of nano-Li_2MnO_3 during charge, where Li^+ diffuse towards the particle surface and Mn^{4+} cations occupy some of the cation vacancies generated from Li^+ extraction. (b) The inwards displacement of Mn^{4+} cations results in the effective extraction of Li_2O from the cathode material, which is electrochemically activated in (c).

Our results showed that, contrary to the general assumption that extra capacities of cation-disordered rock salts are mediated by bulk anionic redox reactions, nano-Li_2MnO_3 acts as an activator to catalyse the reversible formation of electrochemically active Li_2O. The use of full structural (and not just average structural) probes, as well as bulk probes of anionic redox sensitive to only the oxygen bounds to Mn, avoids issues of surface sensitivity of XPS and soft-XAS, which are also sensitive to any other oxygen containing phases like the electrolyte. Based on the success of these techniques to characterize *in operando* and with excellent time resolution and data quality these bulk structural phenomena, the introduced methods should be used to revisit the characterisation of other high capacity cathodes with bulk anionic redox process have been based on TEM, TM K-edge EXAFS, average structure, XPS or DFT calculations, to find conclusive evidence of such reactions.

We further explore the similarities between nano-Li_2MnO_3 and other nanostructured Li–Mn–O cathodes, namely $Li_4Mn_2O_5$. *In operando* Bragg data of the $Li_4Mn_2O_5$ cathode charged to 4.5 V revealed the appearance of broad reflections unindexed by the $Fm\bar{3}m$ space group (see Fig. S16†) that were attributed to unidentified impurities in previous work.[66] The comparison between Fig. 1 and S16† indicates the origin of the diffuse reflections in charged $Li_4Mn_2O_5$ could be instead linked to the formation of a short-range ordered superstructure during cycling. In addition, previous studies of $Li_4Mn_2O_5$ combining main kβ transitions, XANES and EXAFS showed Mn^{3+} irreversibly oxidizes to Mn^{4+} during the first charge.[37] Therefore, $Li_4Mn_2O_5$ could be transformed into a 'nano-Li_2MnO_3 like' material (*i.e.*, with nanodomains of Li/Mn layering and Mn^{4+}) that cycles reversibly between charged and discharged states with a constant oxidation state of Mn^{4+} and charge compensation could be allowed by the reversible formation of Li_2O. Even though Li-rich cation disordered rock-salts are generally associated with the absence of structural transformation during cycling, the chemical ordering observed during charging of $Li_4Mn_2O_5$ warrants further investigations into the chemical ordering of other cation disordered rock-salts showing diffuse nature peaks in their pristine state like $Li_{1.25}Nb_{0.25}Mn_{0.5}O_2$,[67,68] $Li_{1.2}Ti_{0.4}Mn_{0.4}O_2$,[24,69] or $Li_{1.2}Mn_{0.4}Zr_{0.4}O_2$.[69]

Conclusion

This work has determined the true average structure of nano-Li_2MnO_3 as a cubic superstructure with short-range layered ordering in space group $R\bar{3}m$. This ordering has been observed in similar systems, such as $Li_xNi_{2-x}O_2$,[32] or charged $Li_{4-x}Mn_2O_5$ compositions.[66] With respect to previous reports, we have determined there is no unfavourable phase transformations during cycling, in agreement with the absence of the characteristic plateau originated from phase transitions in the electrochemical curve. The large reversible capacity in nano-Li_2MnO_3 is consistent with the high structural reversibility from total scattering and XAS studies carried out under *in operando* conditions. The combination of total scattering, absorption and emission spectroscopy has ruled out O^{2-}/O^{-}, $O^{2-}/O^{1.5-}$, $Mn^{4+}/Mn^{5+/7+}$ (ref. 43) redox or oxygen protonation reactions as suitable mechanisms of charge compensation, and provides a clear evidence of the densification of the Mn-sublattice. The main charge compensation responsible for the extraordinary capacity reversibility in nano-Li_2MnO_3 is the electrochemical activation of Li_2O, with the subsequent stabilization of oxygen radicals at the cathode surface and/or trapping of O_2 molecules within the vacancy clusters. The cathode nanostructuration permits reversible reactions with Li_2O in a controlled manner with high cycling and structural reversibility. Unlike for microstructured cathodes, where compositional changes or decomposition products such as Li_2CO_3 or Li_2O_2 have been ascribed to capacity fading and battery performance deterioration. Other charge compensations mechanisms, with a minor contribution to the overall charge exchanged like the substitution of H_3O^+ for Li^+ should be further investigated by H-NMR.

The full understanding of the charge compensation in nano-Li_2MnO_3 was possible thanks to hard X-rays techniques in XES that provide bulk structural information *in operando*; techniques employing soft X-rays (*e.g.* XPS, or light elements K-absorption edges) may not provide such rich information due to their surface-sensitivity and the requirement for high vacuum environments which may compromise the observed electrochemistry.[70–73]

Conflicts of interest

There are no conflicts to declare.

Acknowledgements

We acknowledge Jean Justine at CRISMAT for technical assistance, Dr James M. Ablet and Dr Jean Pascal Rueff for support during beamtime at GALAXIES-Soleil, Dr Henry Fischer for support during beamtime at D4c-ILL and Diamond Light Source for beamtime under proposals EE20893 and EE20094.

References

1 K. Ozawa, *Solid State Ionics*, 1994, **69**, 212.
2 H. Noh, S. Youn, C. Seung and Y. Sun, *J. Power Sources*, 2013, **233**, 2.
3 H. Yu and H. Zhou, *J. Phys. Chem. Lett.*, 2013, **4**, 1268.
4 C. S. Johnson, N. Li, C. Lefief and M. M. Thackeray, *Electrochem. Commun.*, 2007, **9**, 787.
5 A. R. Armstrong, A. D. Robertson and P. G. Bruce, *J. Power Sources*, 2005, **146**, 275.
6 A. D. Robertson and P. G. Bruce, *Chem. Commun.*, 2002, 2790.
7 R. Benedek, M. M. Thackeray and A. Van De Walle, *Chem. Mater.*, 2008, 5485.
8 A. D. Robertson and P. G. Bruce, *Chem. Mater.*, 2003, 1984.
9 R. Xiao, H. Li and L. Chen, *Chem. Mater.*, 2012, **24**, 4242.
10 H. Chen and M. S. Islam, *Chem. Mater.*, 2016, **28**, 6656.
11 D. Y. W. Yu, K. Yanagida, Y. Kato and H. Nakamura, *J. Electrochem. Soc.*, 2009, **156**, A417.
12 K. Shimoda, M. Oishi, T. Matsunaga, M. Murakami, K. Yamanaka, H. Arai, Y. Ukyo, Y. Uchimoto, T. Ohta, E. Matsubara and Z. Ogumi, *J. Mater. Chem. A*, 2017, **5**, 6695.
13 A. R. Armstrong, M. Holzapfel, P. Novák, C. S. Johnson, S. H. Kang, M. M. Thackeray and P. G. Bruce, *J. Am. Chem. Soc.*, 2006, **128**, 8694.
14 S. A. Freunberger, Y. Chen, Z. Peng, J. M. Gri, L. J. Hardwick, P. Nov and P. G. Bruce, *J. Am. Chem. Soc.*, 2011, **133**, 8040.
15 J.-K. Noh, S. Kim, H. Kim, W. Choi, W. Chang, D. Byun, B.-W. Cho and K. Yoon, *Sci. Rep.*, 2014, **2**, 1.
16 S. Zhao, B. Sun, K. Yan, J. Zhang, C. Wang and G. Wang, *ACS Appl. Mater. Interfaces*, 2018, **10**, 33260.
17 D. Mori, H. Kobayashi, T. Okumura, H. Nitani, M. Ogawa and Y. Inaguma, *Solid State Ionics*, 2016, **285**, 66.
18 E. McCalla, A. M. Abakumov, M. Saubanère, D. Foix, E. J. Berg, G. Rousse, M.-L. Doublet, D. Gonbeau, P. Novák, G. Van Tendeloo, R. Dominko and J.-M. Tarascon, *Science*, 2015, **350**, 1516.
19 J. Hong, W. E. Gent, P. Xiao, K. Lim, D. Seo, J. Wu, P. M. Csernica, C. J. Takacs, D. Nordlund, C. Sun, K. H. Stone, D. Passarello, W. Yang, D. Prendergast, G. Ceder, M. F. Toney and W. C. Chueh, *Nat. Mater.*, 2019, **18**, 256.
20 R. Chen, S. Ren, M. Yavuz, A. A. Guda, V. Shapovalov, R. Witter and H. Hahn, *Phys. Chem. Chem. Phys.*, 2015, **17**, 17288.
21 N. Takeda, S. Hoshino, L. Xie, S. Chen, I. Ikeuchi, R. Natsui, K. Nakura and N. Yabuuchi, *J. Power Sources*, 2017, **367**, 122.
22 J. Lee, D. A. Kitchaev, D. Kwon, C. Lee, J. K. Papp, Y. Liu and Z. Lun, *Nature*, 2018, **556**, 185.
23 N. Yabuuchi, M. Takeuchi, M. Nakayama, H. Shiiba, M. Ogawa, K. Nakayama, T. Ohta, D. Endo, T. Ozaki, T. Inamasu, K. Sato and S. Komaba, *Proc. Natl. Acad. Sci. U. S. A.*, 2015, **112**, 7650.
24 B. Huang, R. Wang, Y. Gong, B. He and H. Wang, *Front. Chem.*, 2019, **7**, 1.
25 M. Freire, N. V. Kosova, C. Jordy, D. Chateigner, O. I. Lebedev, A. Maignan and V. Pralong, *Nat. Mater.*, 2015, **15**, 1.
26 M. Freire, O. I. Lebedev, A. Maignan, C. Jordy and V. Pralong, *J. Mater. Chem. A*, 2017, 21898.
27 M. Oishi, K. Yamanaka, I. Watanabe, K. Shimoda, T. Matsunaga, H. Arai, Y. Ukyo, Y. Uchimoto, Z. Ogumi and T. Ohta, *J. Mater. Chem. A*, 2016, **4**, 9293.
28 G. Assat, A. Iadecola, C. Delacourt, R. Dedryvère and J. M. Tarascon, *Chem. Mater.*, 2017, **29**, 9714.
29 A. J. Perez, D. Batuk, M. Saubanère, G. Rousse, D. Foix, E. Mccalla, E. J. Berg, R. Dugas, K. H. W. Van Den Bos,

M. Doublet, D. Gonbeau, A. M. Abakumov, G. Van Tendeloo and J. Tarascon, *Chem. Mater.*, 2016, **10**, 8278.
30 A. J. Perez, Q. Jacquet, D. Batuk, A. Iadecola, M. Saubanère, G. Rousse, D. Larcher, H. Vezin and M. Doublet, *Nat. Energy*, 2020, **2**, 954.
31 P. E. Pearce, A. J. Perez, G. Rousse, M. Saubanère, D. Batuk, D. Foix, E. McCalla, A. M. Abakumov, G. Van Tendeloo, M. L. Doublet and J. M. Tarascon, *Nat. Mater.*, 2017, **16**, 580.
32 P. T. Barton, Y. D. Premchand, P. A. Chater, R. Seshadri and M. J. Rosseinsky, *Chem.–Eur. J.*, 2013, 14521.
33 D. Balzar, N. Audebrand, M. R. Daymond, A. Fitch, A. Hewat, J. I. Langford, A. Le Bail, D. Louer, O. Masson, C. N. McCowan, N. C. Popa, P. W. Stephens and B. H. Toby, *J. Appl. Crystallogr.*, 2004, **37**, 911.
34 M. G. Tucker, D. A. Keen, M. T. Dove, A. L. Goodwin and Q. Hui, *J. Phys.: Condens. Matter*, 2007, **19**, 335218.
35 S. F. Amalraj, L. Burlaka, C. M. Julien, A. Mauger, D. Kovacheva, M. Talianker, B. Markovsky and D. Aurbach, *Electrochim. Acta*, 2014, **123**, 395.
36 R. D. Shannon, *Acta Crystallogr.*, 1976, **32**, 751.
37 M. Diaz-lopez, Y. Joly, M. Freire, C. Colin, O. Proux, V. Pralong and P. Bordet, *J. Phys. Chem. C*, 2018, **122**, 29586.
38 S. Kobayashi, I. R. M. Kottegoda, Y. Uchimoto and M. Wakihara, *J. Mater. Chem.*, 2004, **1**, 1843.
39 N. Tran, L. Croguennec, M. Mènètrier, F. Weill, P. Biensan, C. Jordy and C. Delmas, *Chem. Mater.*, 2008, **20**, 4815.
40 B. M. Weckhuysen, *Chem. Soc. Rev.*, 2010, **39**, 4754.
41 G. E. Cutsail, N. L. Gagnon, A. D. Spaeth, W. B. Tolman and S. Debeer, *Angew. Chem., Int. Ed.*, 2019, **2**, 9114.
42 U. Bergmann, C. R. Horne, T. J. Collins, J. M. Workman and S. P. Cramer, *Chem. Phys. Lett.*, 1999, **302**, 119.
43 M. D. Radin, J. Vinckeviciute, R. Seshadri and A. Van Der Ven, *Nat. Energy*, 2019, **4**, 639–646.
44 A. I. Palos, M. Anne and P. Strobel, *J. Solid State Chem.*, 2001, **117**, 108.
45 C. M. Fang and G. A. De Wijs, *Chem. Mater.*, 2006, **18**, 1169.
46 B. Ammundsen, D. J. Jones, J. Rozie, L. Agre, H. Berg, R. Tellgren and J. O. Thomas, *Chem. Mater.*, 1998, **10**, 1680.
47 N. Lee, T. Petrenko, U. Bergmann, F. Neese and S. Debeer, *J. Am. Chem. Soc.*, 2010, **132**, 9715.
48 B. Lassalle-kaiser, T. T. B. Iii, V. Krewald, J. Kern, M. A. Beckwith, M. U. Delgado-jaime, H. Schroeder, R. Alonso-mori, D. Nordlund, T. Weng, D. Sokaras, F. Neese, U. Bergmann, V. K. Yachandra, S. Debeer, V. L. Pecoraro and J. Yano, *Inorg. Chem.*, 2013, **52**, 12915.
49 L. M. Housel, L. Wang, A. Abraham, J. Huang, G. D. Renderos, C. D. Quilty, A. B. Brady, A. C. Marschilok, K. J. Takeuchi and E. S. Takeuchi, *Acc. Chem. Res.*, 2018, **51**, 575.
50 M. H. Rossouw, D. C. Liles and M. M. Thackeray, *Mater. Res. Bull.*, 1992, **27**, 221.
51 N. Kijima, Ã. T. Ikeda, K. Oikawa, F. Izumi and Y. Yoshimura, *J. Solid State Chem.*, 2004, **177**, 1258.
52 Y. Pushkar, X. Long, P. Glatzel, G. W. Brudvig, G. C. Dismukes, T. J. Collins, V. K. Yachandra, J. Yano and U. Bergmann, *Angew. Chem., Int. Ed.*, 2010, **49**, 800.
53 J. A. Rees, V. Martin-diaconescu, J. A. Kovacs and S. Debeer, *Inorg. Chem.*, 2015, **54**, 6410.
54 M. M. Thackeray, S.-H. Kang, C. S. Johnson, J. T. Vaughey, R. Benedek and S. A. Hackney, *J. Mater. Chem.*, 2007, **17**, 3112.
55 S. Hy, F. Felix, J. Rick, W. Su and B. J. Hwang, *J. Am. Chem. Soc.*, 2014, 999–1007.
56 M. Diaz-Lopez, P. A. Chater, P. Bordet, M. Freire, C. Jordy, O. I. Lebedev and V. Pralong, *Adv. Energy Mater.*, 2020, **10**, 1902788.
57 J. Hong, H. Lim, M. Lee, S. Kim, H. Kim, S. Oh, G. Chung and K. Kang, *Chem. Mater.*, 2012, **24**, 2692.
58 M. M. O. Thotiyl, S. A. Freunberger, Z. Peng and P. G. Bruce, *J. Am. Chem. Soc.*, 2013, **135**, 494.
59 R. A. House, U. Maitra, M. A. Pérez-osorio, J. G. Lozano, L. Jin, J. W. Somerville, L. C. Duda, A. Nag, A. Walters, K. Zhou, M. R. Roberts and P. G. Bruce, *Nature*, 2020, **577**, 502.
60 M. M. Thackeray, M. K. Y. Chan, L. Trahey, S. Kirklin and C. Wolverton, *J. Phys. Chem. Lett.*, 2013, **4**, 3607.
61 Y. Lim, D. Kim, J. Lim, J. Kim, J. Yu, Y. Kim, D. Byun, M. Cho, K. Cho and M. Park, *J. Mater. Chem. A*, 2015, **3**, 12377.
62 M. Hibino, R. Harimoto, Y. Ogasawara, R. Kido, A. Sugahara, T. Kudo, E. Tochigi, N. Shibata, Y. Ikuhara and N. Mizuno, *J. Am. Chem. Soc.*, 2014, **136**, 488.
63 M. Hibino, T. Kimura, Y. Suga, T. Kudo and N. Mizuno, *Sci. Rep.*, 2012, **2**, 601.
64 Y. Ogasawara, M. Hibino, T. Kudo and N. Mizuno, *J. Electrochem. Soc.*, 2014, **161**, 792.
65 M. Liu, C. Lin, Y. Gu, T. Yang, Z. Gong, G. Yin, X. Gao, X. Zhou and W. Wen, *J. Phys. Chem. C*, 2019, **118**, 14711.
66 M. Freire, M. Diaz-Lopez, P. Bordet, C. V. Colin, O. I. Lebedev, N. V. Kosova, C. Jordy, D. Chateigner, A. L. Chuvilin, A. Maignan and V. Pralong, *J. Mater. Chem. A*, 2018, **6**, 5156.
67 R. Wang, X. Li, L. Liu, J. Lee, D. Seo, S. Bo, A. Urban and G. Ceder, *Electrochem. Commun.*, 2015, **60**, 70.
68 M. A. Jones, P. J. Reeves, I. D. Seymour, M. J. Cliffe, S. E. Dutton and C. P. Grey, *Chem. Commun.*, 2019, **55**, 9027.
69 H. Ji, A. Urban, D. A. Kitchaev, D. Kwon, N. Artrith, C. Ophus, W. Huang, Z. Cai, T. Shi, J. C. Kim, H. Kim and G. Ceder, *Nat. Commun.*, 2019, **10**, 592.
70 Y.-C. Lu, E. J. Crumlin, G. M. Veith, J. R. Harding, E. Mutoro, L. Baggetto, N. J. Dudney, L. Zhi and Y. Shao-Horn, *Sci. Rep.*, 2012, **2**, 7015.
71 E. J. Crumlin, H. Bluhm and Z. Liu, *J. Electron Spectrosc. Relat. Phenom.*, 2013, **190**, 84.
72 N. J. Dudney, Z. Liu and Y. Shao-horn, *J. Phys. Chem. C*, 2013, **117**, 25948.
73 J. Maibach, C. Xu, S. K. Eriksson, J. Åhlund, T. Gustafsson, H. Siegbahn, H. Rensmo, K. Edström and M. Hahlin, *Rev. Sci. Instrum.*, 2015, **86**, 044101.